Normal-mode spectrum of finite-sized granular systems: The effects of fluid viscosity at the grain contacts

John Valenza and David Linton Johnson
Schlumberger-Doll Research, One Hampshire Street, Cambridge, Massachusetts 02139, USA
(Received 21 September 2011; revised manuscript received 17 November 2011; published 12 April 2012)

We investigate the effects of adsorbed films on the attenuative properties of loose granular media occupying a finite-sized rigid container that is open at the top. We measure the effective mass, $\tilde{M}(\omega)$, of loose tungsten particles prepared under two different sets of conditions: (i) We lightly coat tungsten grains with a fixed volume fraction of silicone oil (polydimethylsiloxane, PDMS), where the liquid viscosity is varied for individual realizations, and (ii) in the other set of experiments we vary the humidity. On a theoretical level, we are able to decompose the effective mass into a sum over the contributions from each of the normal modes of the granular medium. Our results indicate that increasing either the PDMS viscosity or the humidity, as the case may be, markedly increases the damping rate of each normal mode relevant to our measurements. However, there is appreciable damping even in the absence of any macroscopic film. With a notable exception in the case of the highest humidity in the humidity-controlled experiments, all the relevant modes are weakly damped in the sense of a microscopic theory based on damped contact forces between rigid particles.

DOI: 10.1103/PhysRevE.85.041302 PACS number(s): 45.70.−n, 46.40.−f, 81.05.Rm

I. INTRODUCTION

Granular media dissipate energy at interparticle contacts. Several studies have focused on using granular media to attenuate structure-borne sound [1,2]. These efforts characterize the properties of the coupled system granular medium plus elastic medium. This approach obscures the property of the granular medium responsible for attenuation. Recently, we established a new technique (described in Sec. II) for characterizing the frequency-dependent effective mass, $\tilde{M}(\omega) \equiv M_1(\omega) + iM_2(\omega)$, of a granular medium filling a rigid cavity [3]. Specifically, we showed that, in many cases of interest, a measurement of $\tilde{M}(\omega)$ can be used to predict accurately the attenuation of a sound-bearing structure containing such grain-filled cavities. This fact allows us to focus on an understanding of what physical properties of the granular medium contribute to $M_2(\omega)$, the attenuative component of $\tilde{M}(\omega)$. This is the purpose of the present article.

If the effects of $\tilde{M}(\omega)$ on the sound-bearing structure are weak, in the sense of first-order perturbation theory, the real part of $\tilde{M}(\omega)$ is simply related to the shift in the resonance frequency of the structure, whereas the imaginary part of $\tilde{M}(\omega)$ directly relates to the reduced quality factor, Q, of that structure [3]. For this reason, we present our results in terms of the real and imaginary parts of $\tilde{M}(\omega)$ rather than the magnitude and phase, say, or the tangent of the loss angle, specific attenuation, and so on.

Previously [3], we established that when the relative humidity is greater than zero, water adsorbed in the region of the grain-grain contacts accounts for the majority of the dissipation in a granular medium. This effect is due to the increase in the volume of adsorbed water with an increase in humidity. Analogous results had been observed by others [4,5] in different situations. In this article, we pursue a further understanding of this effect. Additional experiments consist of a sequence of measurements of $\tilde{M}(\omega)$ in which each sample is lightly coated with silicone oil (polydimethylsiloxane, PDMS) of varying viscosity. The volume of PDMS, $\approx 80\ \mu$L, is chosen to mimic the measured volume of adsorbed water when the humidity is 97%. In both of these systems we are able to deduce the complex-valued resonance frequencies, and residues, of those normal modes which contribute to the effective mass in our accessible frequency range. We follow the trajectories of the normal-mode frequencies of these two systems as we change the strength of the damping mechanism, either the viscosity of PDMS or the relative humidity of water. The results are analyzed within the context of the theory of damped contact forces also developed in this article.

The normal modes of the granular media that we study differ significantly from those under investigation by others in connection with the so-called jamming transition [6]. The effect of gravitational compaction is significant in our systems so they are definitely not homogeneous in any macroscopic sense. As we elaborate in Sec. V, there are very significant surface forces of adhesion in addition to the Hertz-Mindlin ones. This means that unlike the situation in the idealized jamming transition [7] we are able to ensure that our data are in the regime of linear response theory if the amplitude of vibration is small enough. Our measurements of $\tilde{M}(\omega)$ are sensitive only to the subset of granular normal modes for which the displacement goes to zero on the walls of the cavity. Finally, all our measured normal modes are in the long-wavelength limit in the sense that the displacements vary on a scale comparable to the dimensions of the cavity, orders of magnitude larger than the scale of the grains.

The article is organized in the following manner: First, in Sec. II we describe the protocol for preparing a granular medium and, subsequently, measuring $\tilde{M}(\omega)$ (Fig. 1). Next, in Sec. III, we model $\tilde{M}(\omega)$ using the linear equation of motion for each grain, assumed to be rigid. In this model, neighboring grains interact via a complex valued stiffness, the imaginary part of which describes damping. The main result of our model is that $\tilde{M}(\omega)$ is expressible as a sum of simple poles, one for each normal mode in the system. We deduce some properties of the poles (the normal-mode frequencies) and their residues in the limits of weak and of strong damping. Next, in Sec. IV,

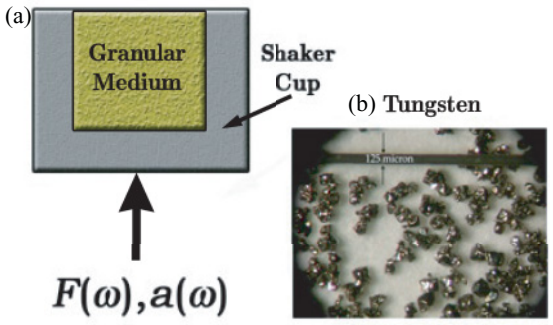

FIG. 1. (Color online) (a) Schematic of the effective mass measurement Eq. (1). (b) Image of tungsten powder used in all $\tilde{M}(\omega)$ measurements. The wire that spans the image is 125 μm wide.

we describe the algorithm for decomposing the $\tilde{M}(\omega)$ data into its normal-mode contributions. This allows us to deduce the complex-valued normal-mode frequencies from the data. In Sec. V, $\tilde{M}(\omega)$ data are analyzed in the context of our theoretical model (Sec. III). Since we are particularly interested in the dissipative capacity of our granular medium, we focus on the behavior of the modes in the system, relative to an increase in damping, and the concomitant effects on M_2. Our findings are summarized in Sec. VI.

II. EXPERIMENT

A cylindrical cavity of diameter 2.54 cm and height 3.07 cm excavated in a rigid aluminum cup is filled with tungsten particles [Fig. 1(b)]. The cup is subjected to a vertical sinusoidal vibration at angular frequency ω; the resulting acceleration is measured with two accelerometers attached to the bottom of the cup on either end of a cup diameter, and the force, $\tilde{F}$, is measured with a force gauge mounted between the shaker and the cup. Taking into account the mass of the empty cup, M_c, we have

$$\tilde{M}(\omega) = \frac{\tilde{F}}{\tilde{a}} - M_c, \tag{1}$$

where $\tilde{a}$ is the average of the acceleration measured by both accelerometers. The amplitude of vibration we use in the experiment is always low enough that the measured $\tilde{M}(\omega)$ is independent of the amplitude.

Each of the tungsten particles consists of four or five equal axis particles, of nominal size 100 μm, fused together. The individual grains are far from being identical; using a microbalance, we measured the mass of 19 of them individually. From this exercise we deduce the average mass of an individual grain to be $m_g = 44.2 \pm 18.0$ μg. Our motivation in using these irregularly shaped particles is because the effective mass is large due to the high density of tungsten.

We are interested in assessing the effect of increasing the dissipation at interparticle contacts, so $\tilde{M}(\omega)$ is measured after mixing the tungsten with PDMS of varying values of DC viscosity (10–60 000 cP). In order to compare the damping effect of viscous PDMS against that of water, we have used a volume of PDMS ($\approx$80 μL) nearly equal to that which we have measured on a 97% relative humidity sample, using a microbalance technique. In order to do this we, first, heavily diluted the PDMS with heptane at a known ratio and measured out a volume corresponding to 80 mg of PDMS. We mixed 100 g of tungsten particles into this solution using a stir plate. After thorough mixing, the majority of heptane evaporates. To ensure that all the heptane evaporates we monitor the mass loss as a function of time subsequent to mixing. We have previously described how we measure the effective mass in a controlled-humidity environment [3].

Due to the propensity of granular media to quickly settle into a metastable state [8], it is very cumbersome to prepare a granular system reproducibly. To ensure comparison of $\tilde{M}(\omega)$ measured on various compositions, it was necessary to identify a handling protocol that yields reproducible behavior. It was previously shown that either mechanical [9] or vibratory compaction [10] is useful for reproducing the state of a granular medium. We previously investigated the efficacy of both techniques for reproducing $\tilde{M}(\omega)$ and found that either is sufficient [3]. The compaction technique is employed for the current study.

The protocol for mechanical compaction consists of using a mechanical testing instrument to impose a sinusoidal stress on the free surface. To promote a uniform imposition of the stress over the free surface of the grains, we use a stainless steel plunger with a rubber pad glued to the bottom surface. First, a static stress of 59.2 kPa is imposed on the granular medium. A sinusoidal stress then is imposed on the system consisting of 200 cycles at a frequency of 0.25 Hz. The stress amplitude is systematically varied between 39.5 and 118.5 kPa, in steps of 39.5 kPa. To prevent unloading the system, the static stress is increased by 39.5 kPa for each equivalent change in stress amplitude. After the maximum stress amplitude is achieved, the procedure is repeated in reverse. So the first two steps consist of increasing, and the second two steps consist of decreasing the stress amplitude. We have limited the maximum stress on the grains to the low value of 118.5 kPa [=1.185 bar], specifically in order to ensure that we are not physically damaging any of the grains. Overall, the system is exposed to 1000 stress cycles (5 sets of 200) at systematically varied stress amplitudes.

III. THEORY

The main purpose of this section is to derive the expansion of the effective mass in terms of the complex-valued normal modes of the confined granular medium, Eq. (22), below. In order to make contact with specific experimental results, we will need the results for weakly damped systems, Eqs. (32) and (33), as well as those for overdamped systems, Eqs. (45) and (39).

Let us model a granular medium held in a cavity in which each grain is considered to be rigid except for the region near the contacts with its neighboring particles. We briefly discussed some of the properties of the effective mass implied by such a model in an earlier publication [3]. Let $\mathbf{X}_i$ be the equilibrium position of the center of mass of the i-th particle, whose mass is m_i, and $\mathbf{u}_i$ be its displacement from equilibrium. Similarly, θ_i is the librational angle of rotation. If two neighboring particles translate or rotate such that their points of contact would move relative to each other there will be a restoring force due to the contact forces. The linearized

equation of motion for the i-th particle is

$$-m_i\omega^2\mathbf{u}_i = -\mathbf{K}_{iw}\cdot[\mathbf{u}_i+\theta_i\times\mathbf{d}_{iw}-\mathbf{W}] + \sum_j \mathbf{K}_{ij}\cdot[\mathbf{u}_j+\theta_j\times\mathbf{d}_{ji}-\mathbf{u}_i-\theta_i\times\mathbf{d}_{ij}] \tag{2}$$

where $\mathbf{d}_{ij}$ is the vector from $\mathbf{X}_i$ to the point of contact with the j-th grain. It is understood that the tensor $\mathbf{K}_{ij}(\equiv\mathbf{K}_{ji})$ is nonzero only for grains actually in contact with each other. (For simplicity we assume there is at most one contact per pair.) Similarly, $\mathbf{d}_{iw}$ and $\mathbf{K}_{iw}$ refer to grains that are in contact with the surfaces of the cavity, whose rigid displacement is $\mathbf{W}$.

The equation of motion for the angular variables is

$$-\omega^2\mathbf{I}_i\cdot\theta_i = -\mathbf{d}_{iw}\times\mathbf{K}_{iw}\cdot[\mathbf{u}_i+\theta_i\times\mathbf{d}_{iw}-\mathbf{W}] + \sum_j \mathbf{d}_{ij}\times\mathbf{K}_{ij}\cdot[\mathbf{u}_j+\theta_j\times\mathbf{d}_{ji}-\mathbf{u}_i-\theta_i\times\mathbf{d}_{ij}] \tag{3}$$

where $\mathbf{I}_i$ is the moment of inertia tensor for the i-th particle.

In the special case that the particles are identical spheres we have $\mathbf{d}_{ij}=(1/2)[\mathbf{X}_j-\mathbf{X}_i]$ and the spring constant tensor may be written in terms of normal (N) and transverse (T) stiffnesses as

$$\mathbf{K}_{ij} = k_{ij}^N\hat{\mathbf{d}}_{ij}\hat{\mathbf{d}}_{ij}+k_{ij}^T[\mathbf{I}-\hat{\mathbf{d}}_{ij}\hat{\mathbf{d}}_{ij}], \tag{4}$$

where $\hat{\mathbf{d}}_{ij}$ is the unit vector and we use dyadic notation. Similarly for the grains in contact with the walls of the cavity. An example here would be Hertz-Mindlin contact forces in which the stiffnesses increase with increasing static compression as happens with increasing depth into a grain-filled cavity, but we also consider forces of adhesion, capillarity, and so on.

It is understood that, generally, each of the elements of the tensors $\mathbf{K}_{ij}$ or $\mathbf{K}_{iw}$ are complex-valued and frequency dependent reflecting the microscopic origin of the dissipation. For the purposes of this section we may take

$$\mathbf{K}_{ij}(\omega) = \mathbf{K}_{ij}^0 - i\omega\mathbf{B}_{ij}, \tag{5}$$

in which the second term describes an interparticle force proportional to the difference in velocity of the two grains. The tensor $\mathbf{B_{ij}}$ is analogous to a dampening parameter. [More generally, Eq. (5) represents simply the first two terms in the Taylor's series expansion of $\mathbf{K}(\omega)$.]

The total force which the cavity exerts on the grains is

$$\mathbf{F} = -\sum_i \mathbf{K}_{iw}\cdot[\mathbf{u}_i+\theta_i\times\mathbf{d}_{iw}-\mathbf{W}] = -\omega^2\sum_i m_i\mathbf{u}_i, \tag{6}$$

where the second equality follows because the interparticle forces cancel, by Newton's third law, as is clear from Eq. (2). Thus, formally, we may deduce each component of the effective mass from Eq. (6). If, for example, we assume the displacement $\mathbf{W}$ is in the z direction, $\mathbf{W}=W\hat{\mathbf{z}}$, and we measure the z component of the force we have the zz component of the effective mass tensor,

$$\tilde{M}_{zz}(\omega) = \sum_i m_i u_{zi}/W. \tag{7}$$

From Eqs. (2) and (3) it is clear that when the frequency tends to zero one has $\lim_{\omega\to0}\mathbf{u}_i=\mathbf{W}$ and $\lim_{\omega\to0}\boldsymbol{\theta}_i=0$. Therefore, in this limit one has, from the second line of Eq. (6), $\mathbf{F}=-\omega^2M_0\mathbf{W}$, where $M_0=\sum_i m_i$ is the total static mass of the grains. Therefore, from the definition of the effective mass, one has the following:

$$\lim_{\omega\to0}\tilde{\mathbf{M}}(\omega) = M_0\mathbf{I}, \tag{8}$$

which seems obvious. In Ref. [3] we also proved

$$\lim_{\omega\to\infty}\mathbf{M}(\omega) = 0, \tag{9}$$

which property we shall use below.

The very simplest explicit form for the effective mass of a granular medium is that appropriate to a single particle of mass m attached to the cavity with spring constant k and damping parameter b, i.e., the simple harmonic oscillator (SHO). As there is only one variable, u, in Eq. (2), for this example, it is obvious that the dynamic effective mass is simply deduced from Eq. (7),

$$\tilde{M}_{\rm SHO} = \frac{-m(k-i\omega b)}{m\omega^2+ib\omega-k} = \frac{A^+}{\omega-\omega_+}+\frac{A^-}{\omega-\omega_-}, \tag{10}$$

where the normal-mode frequencies are the usual,

$$\omega_\pm = \frac{\pm\sqrt{4km-b^2}-ib}{2m}, \tag{11}$$

and the residues of the poles are

$$A^\pm = \mp\frac{k-ib\omega_\pm}{\omega_+-\omega_-}. \tag{12}$$

For future reference we plot the trajectories of the two poles, $\omega_\pm$, as a function of the damping parameter, b, in Fig. 2. We also show the magnitude and phase of the accompanying residues for a few values of b. When $b=0$ one has $\omega_\pm=\pm\omega_0$, where $\omega_0\equiv\sqrt{k/m}$ is the (real-valued) resonance frequency of an undamped SHO. As the damping parameter, b, is increased the resonance frequencies move off the real axis and curve toward the imaginary. Beyond a critical value of b ($=2\sqrt{km}$)

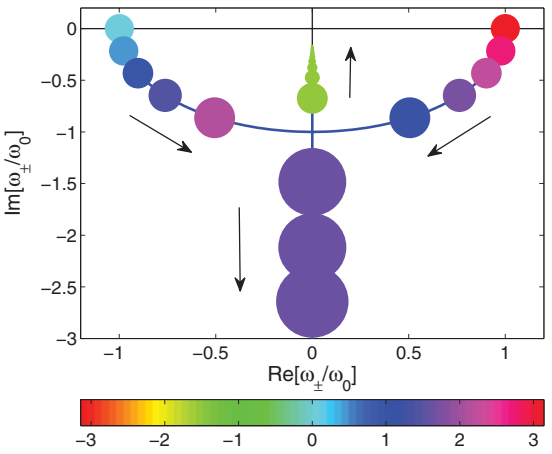

FIG. 2. (Color online) Trajectories of the two normal-mode frequencies of a damped harmonic oscillator in the complex plane, as a function of assumed damping parameter, b. The arrows indicate the direction of movement for increasing values of b. Also shown are the residues of the poles, $A_\pm$, for a few different values of b. The area of each circle is proportional to the magnitude of the residue, $|A_\pm|$. The phase angle of each residue (in radians) is color coded as shown.

both resonances frequencies are purely imaginary valued, as are the residues.

We now show that one can formally write the effective mass for a collection of coupled grains in terms of the normal-mode frequencies of the system in a manner similar to that of the SHO,

$$\tilde{\mathbf{M}}(\omega) = \sum_n \frac{\mathbf{A}_n}{\omega - \omega_n}, \tag{13}$$

where ω_n are the complex-valued frequencies for which Eqs. (2) and (3) have nontrivial solutions when $\mathbf{W}$ is set equal to zero. Each matrix $\mathbf{A}_n$ represents the strength of each resonance. Here, we make this expansion concrete and derive explicit expressions for the residues of the poles (the set $\{\mathbf{A_n}\}$) in terms of the normal modes of the system. We specify to the case of the zz component of the effective mass, in which the acceleration of the cup is in the z direction and the measured force is also in the z direction, i.e., $\tilde{M}(\omega)$ is understood to represent $\tilde{M}_{zz}(\omega)$.

Before we do this, however, we point out for future use that because of the reflection symmetry in the complex plane,

$$\tilde{M}(-\omega^*) = \tilde{M}^*(\omega) \tag{14}$$

(the asterisk denotes complex conjugation), all the normal-mode frequencies occur in pairs, of the form $\pm R - iI$, for which $I \geqslant 0$. This is because $\tilde{M}(\omega)$ is a causal response function, the Fourier transform of a real-valued memory function. (See Sec. IV A of Ref. [3].) In our discussion of the properties of the poles and residues of $\tilde{M}(\omega)$ we focus on those poles which lie in the fourth quadrant of the complex plane, with the understanding that each pole has its mirrored pair in the third quadrant, as required by Eq. (14).

Let us rewrite Eqs. (2) and (3) as

$$H_{ij}u_j = K_{iw}W \quad \{i, j = 1 : 6N\}, \tag{15}$$

where N is the number of particles in the system. Here $\{u_j\}$ represents the set of $3N$ particle displacements ($\mathbf{u}_i$, above) plus the set of $3N$ particle rotation variables, ($\boldsymbol{\theta}_i$). Summation over repeated indices is understood. W is the magnitude of the displacement of the rigid cup, taken to be along the z direction, and K_{iw} represents the generalized spring connecting a grain to the cup. It is equal to zero for those grains not touching the cup wall (i.e., it is zero for most of the grains). Even for those grains in contact with the cup, it is nonzero only if i refers to a coordinate (displacement or rotation) which couples to the z component of the cup displacement. Formally, the individual displacements or rotations are determined by inverting the matrix H_{ij}. The effective mass is determined by Eq. (7):

$$\tilde{M}(\omega) = m_i[H^{-1}]_{ij}K_{jw}, \tag{16}$$

where m_i is the mass of a grain if i refers to the z component of displacement of that grain and is zero otherwise.

The matrix H is complex valued and frequency dependent and it is symmetric ($H_{ij} = H_{ji}$). In general, a non-Hermitian matrix, such as H, may lack the property that its eigenvectors form a complete orthonormal basis [11]. However, according to a recently derived theorem about symmetric complex matrices by Tzeng and Wu [12], there exists $6N$ orthonormal vectors which satisfy a modified eigenvalue-eigenvector problem:

$$H_{ij}e_j^n = \lambda^n e_i^{n*}, \tag{17}$$

where the asterisk denotes complex conjugation. These eigenvectors do form a complete, orthonormal basis:

$$e_j^{n*}e_j^p = \delta_{np}. \tag{18}$$

The eigenvalues, λ^n, are generally complex valued. Tzeng and Wu further showed [12] that the inverse may be written as

$$\mathbf{H}^{-1} = \sum_n \frac{1}{\lambda^n}\mathbf{e}^n\mathbf{e}^n, \tag{19}$$

where we are using dyadic notation. Therefore, from Eq. (16),

$$\tilde{M}(\omega) = \sum_n \frac{m_i e_i^n(\omega)\, e_j^n(\omega)K_{jw}(\omega)}{\lambda^n(\omega)}. \tag{20}$$

A normal mode of the granular medium is a solution to Eqs. (2) and (3) in which there is no forcing by the cup motion, i.e., when $\mathbf{W} \equiv 0$. They occur at specific complex-valued frequencies $\{\omega_m\}$. The corresponding displacements or rotations correspond to an eigenvector of H whose eigenvalue is zero, i.e., $\lambda^n(\omega_m) = 0$. For frequencies in the vicinity of ω_m we may write,

$$\lambda^n(\omega) = \alpha^m(\omega - \omega_m) + O(\omega - \omega_m)^2. \tag{21}$$

If we substitute the first term of Eq. (21) into Eq. (20), and evaluate each eigenvector at the corresponding normal-mode frequency, we get

$$\tilde{M}(\omega) = \sum_m \frac{A_m}{\omega - \omega_m}, \tag{22}$$

in which the residue is

$$A_m = \frac{m_i e_i^m(\omega_m)\, e_j^m(\omega_m)K_{jw}(\omega_m)}{\alpha^m}. \tag{23}$$

In Eq. (22) it is understood that the sum is over all normal modes in the system, which is those eigenvectors of H for which the corresponding eigenvalue is zero. Thus, the summation over n, the eigenvalue counting index, is superfluous and we drop it.

Although Eq. (21) is an approximation, Eq. (22) is an exact representation of the full frequency dependence of the effective mass, Eq. (7) [or Eq. (16) or Eq. (20)]. This is because the former represents a summation over all the poles and residues of the latter. Therefore, the difference between the two functions is analytic everywhere in the complex plane. The only function that is analytic everywhere in the complex plane is the constant function. That constant must be zero because each of the equations (16) and (22) tends to zero as ω tends to infinity. QED

The quantity α^m can also be expressed more cleanly in terms of the eigenvectors by means of a perturbation theory where $\Delta\omega = \omega - \omega_m$ is the small parameter as follows:

$$\mathbf{H}(\omega) = \mathbf{H}(\omega_m) + \frac{\partial \mathbf{H}}{\partial \omega}\Delta\omega, \quad \lambda(\omega) = 0 + \Delta\lambda\ [=\alpha^m\ \Delta\omega],$$
$$\mathbf{e}^m(\omega) = \mathbf{e}^m(\omega_m) + \Delta\mathbf{e}^{\mathbf{m}}. \tag{24}$$

By substituting Eqs. (24) into Eq. (17), and collecting all the terms that are first order in $\Delta\omega$, we may solve for α^m as follows:

$$\alpha^m = e_i^m(\omega_m)\left.\frac{\partial H_{ij}}{\partial\omega}\right|_{\omega_m} e_j^m(\omega_m). \tag{25}$$

Therefore, we may rewrite Eq. (23) as

$$A_m = \left.\frac{m_i e_i^m\, e_j^m K_{jw}}{e_k^m \frac{\partial H_{kl}}{\partial\omega} e_l^m}\right|_{\omega_m}. \tag{26}$$

The implications of Eqs. (22) and (26) are that the entire frequency dependence of $\tilde{M}(\omega)$ can be expressed in terms of the normal-mode frequencies, $\{\omega_n\}$, and the normal-mode coordinates, $\{\mathbf{e}^m(\omega_m)\}$. In practice (Sec. V), experimental data can be understood in terms of a relatively small such number of these, namely those whose normal-mode frequencies are relatively near the frequency range of interest.

In Appendix A we demonstrate the general results of this section as applied to a specific example of a multiparticle system in which we derive analytic expressions for $\tilde{M}(\omega)$, ω_m, and A_m. In the next subsections we derive some results applicable to cases in which the attenuative part of the spring constant is small and in which it is large.

We note in passing that as the size of $\mathbf{H}$ is $6N \times 6N$ the expression for the determinant is a polynomial of degree $12N$ in ω. This means that, within the context of the rigid grain model, there are $12N$ normal-mode frequencies, some of which may be purely imaginary and the others of which occur in pairs, $\omega_n^{\pm} = \pm a - i \mid b \mid$. For the granular media samples we are considering here, $N \approx 2 \times 10^6$.

A. No attenuation

First, we assume the damping components of all the springs vanish: $\mathbf{B}_{ij} \equiv 0$. The matrix H is now symmetric and real so all the eigenvalues are real for real values of frequency ω. Thus, the normal-mode frequencies are real valued. Let us call them ω_m^0. Without loss of generality the normal-mode displacements or rotations, $\mathbf{e}^{m0}$, may also be taken to be real valued. The residue of the pole, A_m^0, is real valued.

The expression (25) also simplifies. The only contribution to this expression is from the inertial terms which are shown in Eqs. (2) and (3). We find

$$\alpha^{m0} = -2\omega_m^0 e_i^{m0}\, I_{ij}\, e_j^{m0}, \tag{27}$$

where the matrix I is a block-diagonal matrix; $I_{ii} = m_i$ if i refers to a coordinate displacement. If i and j refer to rotation coordinates of the same particle, then I_{ij} is that component of the moment of inertia tensor for the grain in question. All other elements of I are equal to zero. In the very, very special case that the particles are identical point masses of mass m (or identical spherical particles with central forces only between grains) we have

$$\alpha^{m0} = -2m\omega_m^0. \tag{28}$$

B. Weak attenuation

Let us now assume that the damping component of each spring is nonzero but also that it is small as compared to the real part,

$$\mathbf{K}_{ij}(\omega) = \mathbf{K}_{ij}^0 - i\xi\omega\mathbf{B}_{ij}. \tag{29}$$

[An equivalent expression holds for the relevant grain-wall springs, $\mathbf{K}_{iw}(\omega)$.] The smallness parameter, $\xi \ll 1$, is a stand-in for the viscosity, say. We may compute the effect of this new term using first-order perturbation theory.

In a manner analogous to the derivation of Eqs. (24) it is simple to derive the change in the eigenvalue, $\Delta\lambda(\omega)$. The result is

$$\lambda(\omega) = \alpha^{m0}\left(\omega - \omega_m^0\right) - i\xi\omega\, e_i^{m0}\, B_{ij}\, e_j^{m0} + O(\xi^2). \tag{30}$$

The new normal-mode frequency, ω_m, defined by $\lambda(\omega_m) = 0$, is

$$\omega_m = \omega_m^0 - \xi\,\frac{i}{2}\,\frac{e_i^{m0}\, B_{ij}\, e_j^{m0}}{e_i^{m0}\, I_{ij}\, e_j^{m0}} + O(\xi^2), \tag{31}$$

or, more succinctly,

$$\omega_m(\xi) = \omega_m^0 - i\,\xi\,\gamma_m + O(\xi^2). \tag{32}$$

To first order in the damping considered as a small parameter, there is no change in the real part of the resonance frequency; the imaginary part is proportional to ξ and it is negative ($\gamma_m > 0$), as required by causality considerations.

Similarly, there is a first-order change in the residue of the pole, which change is also purely imaginary,

$$A_m(\xi) = A_m^0 + i\,\xi\,C_m + O(\xi^2). \tag{33}$$

The contribution of said pole to the imaginary part of the effective mass broadens it from its initial δ function into a skewed Lorentzian, but the area under the peak does not change to first order in ξ:

$$\int_{-\infty}^{\infty} \mathrm{Im}\left[\frac{A_m(\xi)}{\omega - \omega_m(\xi)}\right] d\omega = -\pi A_m^0 + O(\xi^2). \tag{34}$$

Thus, if there is a number of these sharp resonances in some (real) frequency band, $\omega_L < \omega < \omega_U$, which is wide compared to the width of each of the peaks, $[\omega_U - \omega_L \gg \max(\xi\gamma_m)]$, then Eq. (34) shows that the average value of the imaginary part of the effective mass over that band does not change as the attenuation mechanism is increased (to first order in ξ), though we may expect the rms deviation from the mean to decrease as the granular damping increases. The maximum of each peak is reduced but that reduction is compensated by an increase in the width of the peak. We will see in our own experimental data that these results may hold even in situations in which the individual resonances are so closely spaced that they are difficult to resolve.

C. Damping: No stiffness

Next we consider the opposite limit of that considered in Sec. III A. Let us suppose that the damping part of each spring is so large that we may sensibly neglect the real part of the spring constant,

$$\mathbf{K}_{ij}(\omega) = -i\omega\xi\mathbf{B}_{ij}. \tag{35}$$

(Here ξ is not necessarily a small parameter; we introduce it to show how the various quantities scale as the attenuation

mechanism increases.) This means that the matrix operator, H, is of the form,

$$H_{ij} = -\omega^2 I_{ij} + i\ \xi\ \omega\ G_{ij}, \tag{36}$$

where the elements of G_{ij} are real and symmetric. For values of ω which lie on the imaginary axis, ($\omega = i\beta$), H is a real and symmetric matrix. Therefore, its eigenvalues, $\lambda(i\beta)$ are real valued. All the normal-mode frequencies, ω_m, are imaginary,

$$\omega_m = -i\xi\beta_m, \tag{37}$$

in which causality requires that $\beta_m > 0$. The normal-mode coordinates, $e_i^m(\omega_m)$, are real valued.

The quantity α_m may be evaluated via Eq. (25) as follows:

$$\alpha_m = i\xi e_i^m [2\beta_m I_{ij} + G_{ij}] e_j^m = i\xi\beta_m e_i^m I_{ij} e_j^m. \tag{38}$$

The residue of the pole, Eq. (23), is also imaginary and scales with ξ,

$$A_m = i\xi a_m. \tag{39}$$

The contribution of one of these poles to the effective mass,

$$\tilde{M}_m(\omega) = \frac{i\xi a_m}{\omega + i\xi\beta_m}, \tag{40}$$

has a very broad peak in the imaginary part which peaks at $\omega = \xi\beta_m$. Its contribution to the average over a frequency band $[\omega_L, \omega_U]$ is

$$\int_{\omega_L}^{\omega_U} \mathrm{Im}[\tilde{M}_m(\omega)]\, d\omega = \frac{\xi a_m}{2} \ln\left(\frac{\omega_U^2 + \xi^2\beta_m^2}{\omega_L^2 + \xi^2\beta_m^2}\right). \tag{41}$$

If that frequency band is large enough and covers the main peak ($0 < \omega_L \ll \xi\beta_m \ll \omega_U$), one has

$$\int_{\omega_L}^{\omega_U} \mathrm{Im}[\tilde{M}_m(\omega)]\, d\omega = \xi a_m \ln\left[\frac{\omega_U}{\xi\beta_m}\right]. \tag{42}$$

This result demonstrates an intuitively obvious situation: If the damping of the grain-grain contacts are large enough that one of the normal modes is overdamped, then this pole contribution to the average of the imaginary part of the effective mass, taken over a frequency range that includes the broad maximum at $\xi\beta_m$, scales linearly with the strength of the damping parameter, modulo a logarithmic correction.

D. Damping: Weak stiffness

Finally, we consider the situation that is the obverse of that in Sec. III B. The grain-grain, or grain-wall, springs are given by Eq. (29) in which $1/\xi$ is the small parameter for this perturbation theory. We now derive modifications to Eqs. (37)–(39) correct through order ξ^{-1}. We consider the eigenvalues, $\lambda^n(\omega)$, of Eq. (17) which now takes the form analogous to Eq. (36),

$$H_{ij} = -\omega^2 I_{ij} + i\ \xi\ \omega\ G_{ij} - L_{ij}. \tag{43}$$

The new term, L_{ij}, represents the effect of the real-valued spring constants $\mathbf{K}_{ij}^0$ in Eq. (5). This matrix is real valued and symmetric. We treat this new term, as well as those proportional to $\delta\omega \equiv \omega - \omega_m$ from the first two terms, to first order in perturbation theory. The result is

$$\lambda(\omega) = \alpha_m(\omega + i\xi\beta_m) - \frac{e_i^{m0} L_{ij} e_j^{m0}}{e_l^{m0} e_l^{m0}} + O(\xi^{-1}), \tag{44}$$

where α_m is given by Eq. (38). The new normal-mode frequencies are defined, as usual, by $\lambda(\omega_m) = 0$. We find the following:

$$\omega_m = -i\xi\beta_m\ - i\frac{e_i^{m0} L_{ij} e_j^{m0}}{\xi\beta_m e_i^m I_{ij} e_j^m} + O(\xi^{-2}). \tag{45}$$

To this level of perturbation theory, the residue, A_m, is also purely imaginary. This result suggests that for weak-enough spring stiffness values the normal-mode frequencies are purely imaginary; we show an example of this behavior in experimental data analyzed in Fig. 12. What we have rigorously demonstrated, however, is that this is certainly true to first order in $1/\xi$, the ratio of stiffness effects to damping effects.

The picture that emerges from this section is as follows: If damping of each grain-grain, or grain-wall, contact is completely negligible, the normal-mode frequencies occur as real-valued pairs, $\pm\omega_n$. The corresponding residues, A_n, are also real valued. If each contact spring acquires a small damping constant, as in Eq. (29), then each normal-mode frequency acquires a negative imaginary part: $\pm\omega_n \to \pm\omega_n - i\gamma_n$. As the damping of each spring is increased further, $|\mathrm{Im}[\omega_n]|$ continues to increase and $|\mathrm{Re}[\omega_n]|$ decreases until the mirrored pair meet on the negative imaginary axis, which occurs for some critical value of the damping. For values of the damping parameter larger than this critical value, the normal-mode frequencies are purely imaginary valued. Just this behavior is seen in the SHO example discussed in Eqs. (11) and (12) and plotted in Fig. 2. For the general case of a collection of interacting particles we have, however, proved this hypothesis only for very large values of the damping and for very small ones. In Appendix B we give another example of a simple model which also exhibits such behavior.

IV. DECOMPOSITION OF EXPERIMENTAL DATA INTO NORMAL-MODE CONTRIBUTIONS

We have measured the effective mass at a series of discrete frequencies: $[M_i = \tilde{M}(\omega_i^e) : i = 1, N_f]$. (Typically, $N_f \approx 1500$.) In this section we show how we can determine the poles $\{\omega_n\}$ and their residues $\{A_n\}$ from the data. The first step is to analytically continue the discrete data into the complex ω plane using a rational function technique [13], as we have described previously [3]. The true causal response function has the reflection property that

$$\tilde{M}(-\omega^*) \equiv \tilde{M}^*(\omega), \tag{46}$$

where the asterisk denotes complex conjugation. This is because $\tilde{M}(\omega)$ is the Fourier transform of a real-valued kernel in the time domain [3]. In order to preserve this symmetry, we extend the experimental data to negative real-valued frequencies by use of the following rule: $\tilde{M}(-\omega_i^e) = \tilde{M}^*(\omega_i^e) : i = 1, N_f$. Furthermore, we include in the data set the value of the static mass on the granular medium, $M_0 = \tilde{M}(0)$, which is real valued. The resulting rational function, which we shall denote as $\tilde{M}_{\mathrm{RF}}(\omega)$, has the following properties:

(i) It passes through each original experimental datum exactly. $[\tilde{M}_{\mathrm{RF}}(\omega_i^e) \equiv M_i : i = 1, N_f]$.

(ii) It obeys the reflection property, Eq. (46).

(iii) Because the extended data set now has an odd number of data points, $2N_f + 1$, the order of the polynomial in the numerator and in the denominator of the rational function are equal to each other (and equal to N_f). This, in turn, guarantees that the rational function approximation to $\tilde{M}$ and to $1/\tilde{M}$ (which we denote as $[\tilde{M}^{-1}]_{\rm RF}$) are reciprocals of each other for all complex values of ω as follows:

$$\tilde{M}_{\rm RF}(\omega) \equiv \mathbf{[}[\tilde{M}^{-1}]_{\rm RF}(\omega)\mathbf{]}^{-1}. \tag{47}$$

If, instead, the total number of data points used is an even number, then, in general, Eq. (47) will be violated to some extent. It is for this reason that we include the static mass as one of the data points.

Our procedure consists of searching for a zero, call it ω_1, in the complex plane of the function $[\tilde{M}^{-1}]_{\rm RF}$ which we do using Muller's method [13] as we have done before in a different context [3]. We take ω_1 as an approximation to a pole in $\tilde{M}(\omega)$. Next, we form the rational function approximation $A_{\rm RF}(\omega) \equiv [(\omega - \omega_1)\tilde{M}]_{\rm RF}(\omega)$. The residue of this pole is

$$A_1 = A_{\rm RF}(\omega_1), \tag{48}$$

as is obvious from Eq. (22). Because of the reflection symmetry there is another pole at $\omega_{-1} \equiv -\omega_1^*$ having a residue $A_{-1} \equiv -A_1^*$. We define a new set of data points $[(\omega_i^e, M_i^{(2)})\ i = -N_f, N_f]$ by subtracting these pole contributions from the extended data set as follows:

$$\tilde{M}_i^{(2)} = M_i - \frac{A_1}{\omega_i^e - \omega_1} - \frac{A_{-1}}{\omega_i^e - \omega_{-1}} \quad i = -N_f, N_f. \tag{49}$$

We then treat this new data set in the same manner as the original one in order to find a second pole, ω_2, and its residue, A_2. We subtract these new pole contributions from $M_i^{(2)}$ and we iterate the process until we have uncovered all the pole contributions that are relevant to our experimental data.

As discussed in Sec. III, there may be normal modes which are overdamped. Such frequencies lie on the negative imaginary axis: $\omega_k = -i|\omega_k|$. Because of the reflection symmetry, $\tilde{M}_{\rm RF}(\omega)$ is real valued for ω on the imaginary axis. Thus, it is easy enough to identify such pole(s) simply by plotting $\tilde{M}_{\rm RF}(-i|\omega|)$.

In order to test whether this procedure can actually be expected to work correctly, especially for those poles well off the real axis, we have applied it to a test function whose resonant frequencies and residues can be determined analytically, in Appendix B. There, we see that the algorithm is able to accurately deduce the normal-mode frequencies and their residues as long as they are not too far from the region where we have input data.

V. RESULTS AND DISCUSSION

In this section we, first, discuss our results on the tungsten particles coated with different PDMS of varying viscosities, and then we discuss our results on (clean) tungsten particles measured at different humidity values.

A. PDMS-coated grains

The tungsten granules for each sample were coated with a total of 80 mg of PDMS and then they were mechanically compacted into a rigid cup. In Fig. 3 we show a comparison of our measured effective mass data against that reconstructed from the pole decomposition scheme described in Sec. IV in which the PDMS DC viscosity is 99.7 cP. The locations and residues of the corresponding poles are plotted in Fig. 4, with the understanding that each pole has its mirrored counterpart in

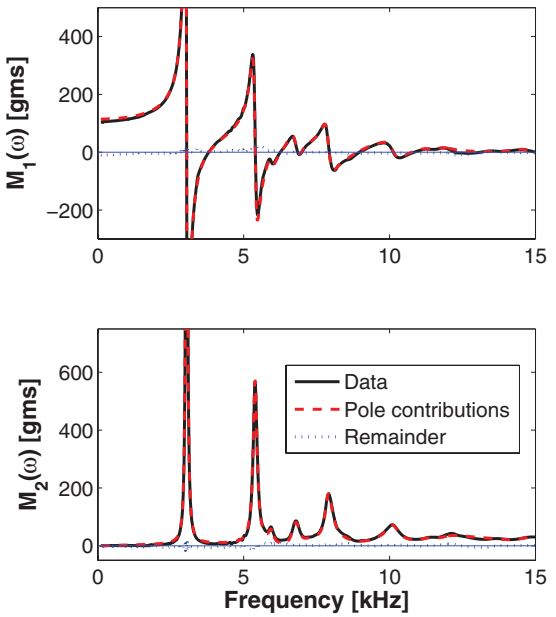

FIG. 3. (Color online) Comparison of measured effective mass data against that deduced from the pole decomposition algorithm of Sec. IV. The grains were coated with 80 mg of 99.7-cP PDMS before compaction into the cavity. The difference between the data and the pole decomposition is quite small everywhere.

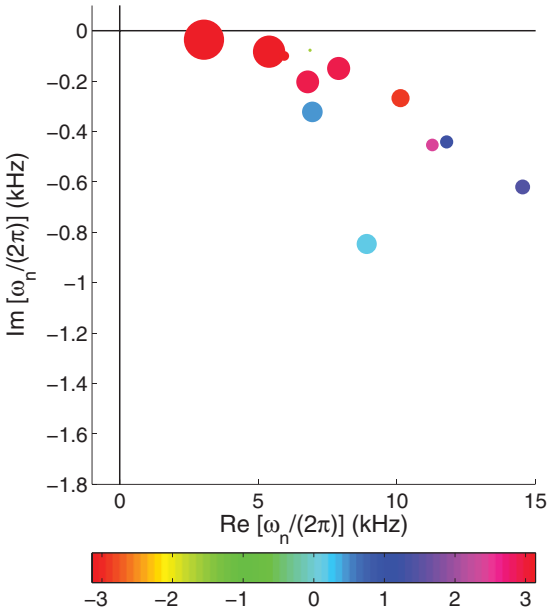

FIG. 4. (Color online) Locations of the normal-mode frequencies which contribute to the pole expansion of the effective mass data in Fig. 3. The area of each circle is proportional to the magnitude of the residue, $|A_n|$. The phase angle of each residue (in radians) is color coded as shown.

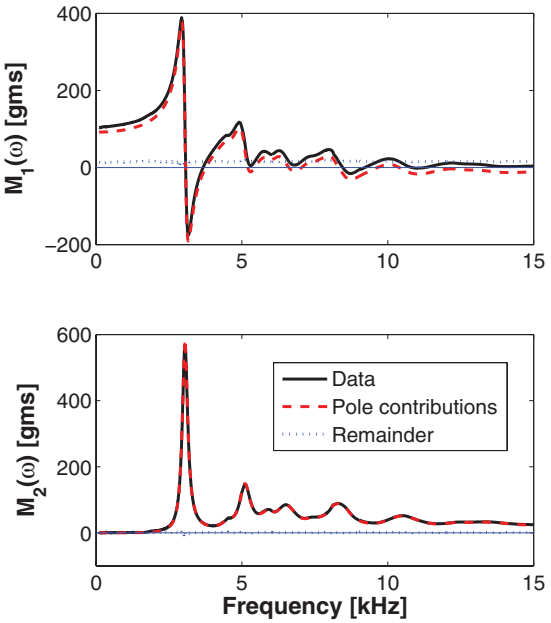

FIG. 5. (Color online) Effective mass data and its pole decomposition for grains coated with 894-cP PDMS. Same conventions as in Fig. 3. Here, the remainder is larger than in Fig. 3 but it is nearly a real-valued constant.

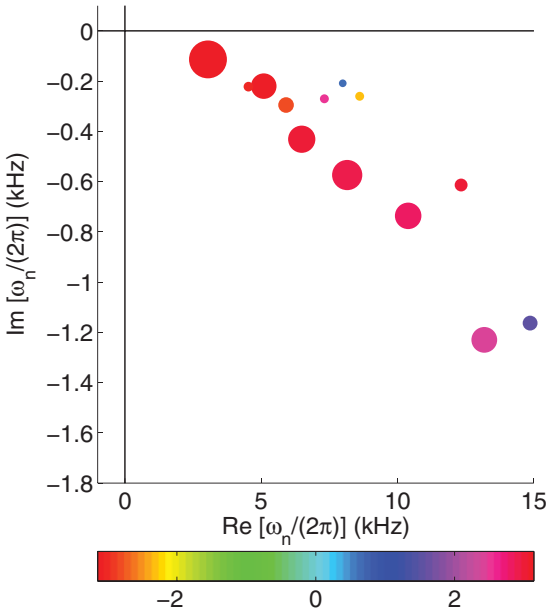

FIG. 6. (Color online) Locations of the normal-mode frequencies for the 894-cP-coated grains of Fig. 5. Same conventions as in Fig. 4. The set of the normal-mode frequencies has moved further from the real axis, relative to those in Fig. 4.

the third quadrant. We see that the data can be well represented in terms of a relatively few pole contributions with a remainder that is quite small. Moreover, all of the poles are located nearly on the real axis: $|\mathrm{Im}[\omega_n]| \ll \mathrm{Re}[\omega_n]$.

The results of Fig. 4 imply that these modes are weakly damped as discussed in Sec. III B. Accordingly, in Fig. 5 we show our results for the effective mass of tungsten granules prepared as before but with a much higher DC viscosity, 894-cP PDMS. The corresponding pole locations are shown in Fig. 6.

It is apparent from a visual comparison of Figs. 3 and 5 that the normal modes of the latter are significantly more damped than those of the former. Indeed, this behavior is borne out quantitatively in a comparison of Figs. 4 and 6. We have repeated the measurements of the effective mass using PDMS fluids with a wide range of DC viscosity values, always holding to 80 mg coating. Some properties of the fundamental resonance mode are shown in Fig. 7.

We see from this figure that the real part of the resonance frequency as well as the real part of the residue are nearly constant, even though we have varied the DC viscosity of the coating fluid over five orders of magnitude. In addition, the damping component of this mode increases before leveling off when the DC viscosity is greater than 1000 cP. This initial increase is linear, as we demonstrate in Fig. 8.

We use the compaction protocol in order to produce granular samples which are "identical," except for the variation in viscosity of PDMS or humidity. Obviously, this is not perfect and we see there is some scatter in the plots. Even so, we see that the behavior of the three quantities plotted in Fig. 7 is fully consistent with the theoretical predictions of a weakly damped system, Eqs. (32) and (33), in which ξ is linearly related to the viscosity, η, of the grain-coating PDMS. We may say that $\xi = a + b\eta$ in which a represents other attenuation mechanisms that are unrelated to the viscosity of the coating fluid. For fluids whose DC viscosity is greater than 200 cP we

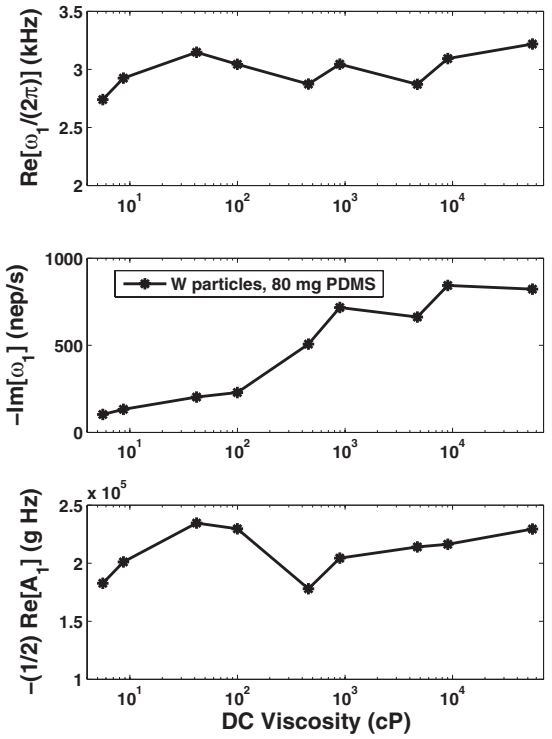

FIG. 7. Properties of the fundamental resonance in the effective mass of tungsten granules coated with 80 mg of PDMS of different DC viscosity values. (Top) The real part of the resonance frequency. (Middle) The imaginary part. (Bottom) The real part of the residue of that mode's contribution to the effective mass.

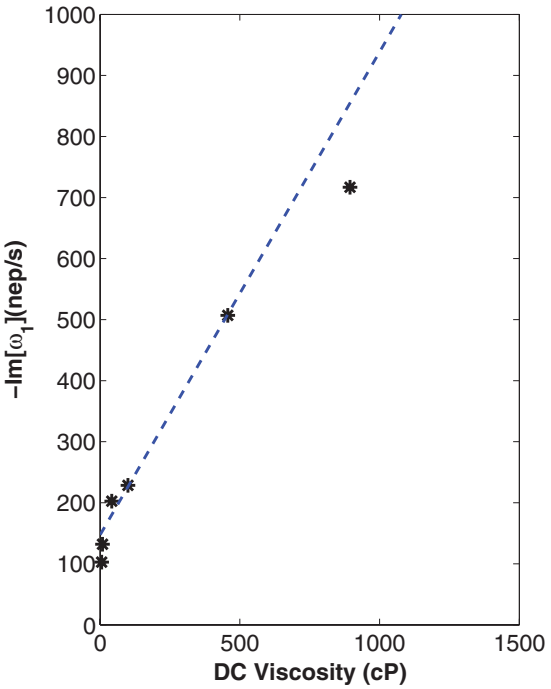

FIG. 8. (Color online) Same data as in the middle part of Fig. 7 but plotted on a linear scale. The dashed curve is a straight line fit to the data points 2–5.

may say that viscous damping due to the adsorbed films is the dominant mechanism of attenuation in these systems.

Why do the data for the damping rates of the fundamental mode, $-\mathrm{Im}[\omega_1]$, level off as the DC viscosity is increased beyond, say, 1000 cP? What is happening is that these fluids are significantly non-Newtonian, especially for those of the higher-viscosity values. From Fig. 14 of Barlow *et al.* [14], we see that as the low-frequency viscosity is increased (by increasing the molecular chain length) the shear modulus asymptotes to a complex-valued plateau; the frequency at which this happens decreases with increasing chain length. For a Newtonian fluid, the shear modulus is purely imaginary and is related to the (frequency independent) viscosity by

$$\tilde{G}_{\mathrm{newt}}(\omega) = -i\omega\eta, \tag{50}$$

where η is the (Newtonian) viscosity. According to the PDMS data of Ref. [14], increasing the DC viscosity beyond 1000 cP does not affect the shear modulus for frequencies greater than about 1 kHz. It is equivalent to saying that the viscosity is complex valued and frequency dependent but does not change with increasing PDMS chain length for frequencies greater than 1 kHz. That is, in the context of our theoretical model, Eq. (32), ξ is not increasing with increasing PDMS chain length beyond a certain limit.

In such cases, where the rheological behavior of the PDMS is relevant in our frequency range, Eq. (5) is modified, viz.,

$$\mathbf{K}_{ij}(\omega) = \mathbf{K}^0_{ij} + \mathbf{C}_{ij}\tilde{G}(\omega), \tag{51}$$

where $\tilde{G}(\omega)$ is the complex-valued frequency-dependent shear modulus of the liquid and $\mathbf{C}_{ij}$, which is real valued, depends on the geometry of the adsorbed film in the contact region; when $\tilde{G}(\omega)$ is given as Eq. (50), then Eq. (51) reduces to Eq. (5). The real part of $\tilde{G}(\omega)$ may be comparable to the imaginary part for these rheological liquids but this does not manifest itself as a measurable shift in the real part of the resonance frequency in Fig. 7. The second term in Eq. (51) is always small compared to the first for the fundamental modes of these PDMS wetted systems. Moreover, the surface tension for all these PDMS liquids is about the same: 20 ± 1 dyn/cm [15]. Thus, we do not expect, and we do not observe, any change in the fundamental resonance frequency due to changes in the surface tension from one PDMS fluid to another.

We could, in principle, analyze each of the other modes contributing to $\tilde{M}(\omega)$ in the same way but we prefer to take a statistical approach as there are so many resonances and it is not obvious which resonance frequency at one viscosity connects with which at another. Let us define the average $\langle M_2 \rangle$ as

$$\langle M_2 \rangle = \sum_{i=1}^{N_f} M_2(f_i)\ /N_f \tag{52}$$

and the RMS deviation, ΔM_2, as

$$\Delta M_2 = \sqrt{\langle M_2^2 \rangle - \langle M_2 \rangle^2}. \tag{53}$$

(For all of the data reported here, $f_1 = 105$ Hz, $f_N = 15005$ Hz, and $N_f = 1491$.) These quantities are plotted in Fig. 9 as a function of the DC viscosity of the PDMS fluids. From the theoretical arguments presented in Eq. (34) for a weakly damped system we would expect $\langle M_2 \rangle$ to be independent of the DC viscosity. Furthermore, because each resonance peak broadens and widens, we would expect ΔM_2 to decrease with increasing DC viscosity. Both of these behaviors are seen in the data, up to the point where the AC viscosity of PDMS saturates.

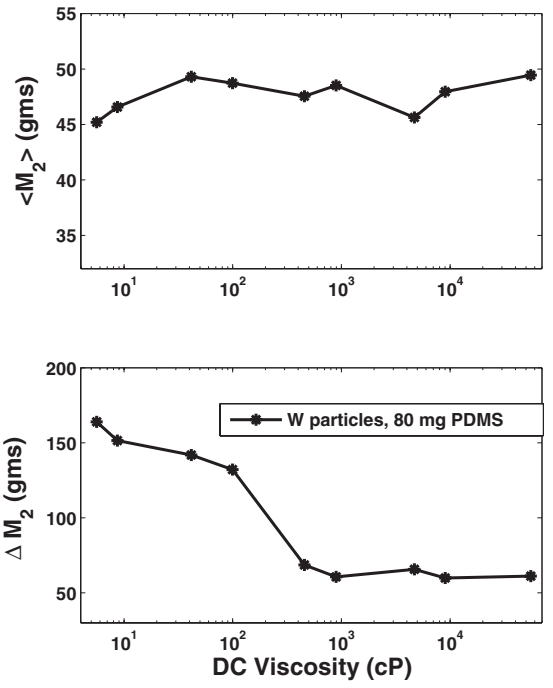

FIG. 9. Statistical properties of M_2 computed over the frequency range of the experiment as a function of PDMS DC viscosity. (Top) Average; (bottom) standard deviation.

Thus, our conclusion is that the attenuative properties of these PDMS-coated granular media are dominated by the viscous properties of the fluid. Furthermore, we conclude that the damping is "weak" in the sense discussed in Sec. III B.

B. Effects of humidity

In our previous publications (Ref. [3] and references therein) we have established that the film of adsorbed water which coats grains at any finite humidity is largely responsible for the attenuation mechanism in otherwise uncoated tungsten granules. In this subsection we pursue this a bit further using the analysis we have developed in this paper.

The grains were cleaned by rinsing, first in acetone and then in isopropyl alcohol. The powder then was subsequently baked in a 60 °C oven for 7 days in order to reduce the humidity to nearly zero. On removal from the oven they were poured loosely into the shaker cup and allowed to cool to room temperature in a glove box held at 0% relative humidity for 24 h before the first effective mass measurements were made. Subsequently, the humidity was raised using pans of different salt-saturated solutions to control the humidity, as we have described previously [3]. Inasmuch as we are interested in studying the effects of humidity, starting with the oven dried sample, we did *not* use the compaction protocol here but just loosely compacted the grains by tapping on the shaker cavity. (It is not possible for us to compact the sample without exposing it to room conditions.) Consequently, as we shall see, the fundamental resonance frequencies we measure for this suite of samples are significantly lower than those we reported earlier [3] using the compaction protocol.

After each change of humidity the system stabilized for at least 24 h prior to measuring the associated effective mass. Analogously to Fig. 7, we plot some properties of the fundamental resonance as a function of equilibrium humidity in Fig. 10. The average and the standard deviation of the imaginary part of $\tilde{M}(\omega)$ are plotted in Fig. 11 as a function of humidity. Within the context of our theoretical model we may say that the damping parameter, ξ, scales monotonically with the amount of adsorbed water. Roughly speaking, the behaviors of Figs. 10 and 11 are similar in kind to those of Figs. 7 and 9. Thus, the behavior of these systems is also consistent with the weak damping limit discussed above. We make the following observations:

(i) There are two fundamental resonances of the "zero" humidity sample overlapping each other, one narrow and one broad. Both modes are shown in Fig. 10. The decay rate of the narrower one, $-\mathrm{Im}[\omega_1] = 183$ nep/s, is comparable to the value implied by an extrapolation of the viscosity data to zero viscosity implied by Fig. 8 (≈140 nep/s). We conclude that this value represents an attenuation mechanism not related to the bulk viscosity of the adsorbed film, similarly, in kind, to what has been observed in the acoustic attenuation in rocks [16].

(ii) The total absorption of these two resonances, i.e., the sum $-(1/2)\mathrm{Re}[A_1 + A_2] = 9.4 \times 10^4$ (g Hz), is approximately equal to the expected value of the nonzero humidity data extrapolated to zero humidity.

(iii) The attenuation of the fundamental mode shown in Fig. 10 attains values considerably larger than those for the PDMS-coated grains, despite the fact that all the data in

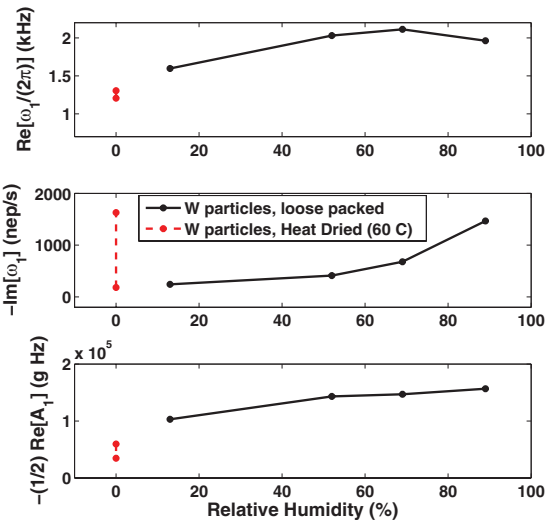

FIG. 10. (Color online) Properties of the fundamental resonance in the effective mass of tungsten granules as a function of humidity. (Top) The real part of the resonance frequency. (Middle) The imaginary part. (Bottom) The real part of the residue of that mode's contribution to the effective mass. The data were taken at room temperature.

Fig. 7 are for liquids considerably more viscous than water ($\eta = 1$ cP). Using a microbalance we monitored the mass uptake of 100 g of these tungsten particles at 97% relative humidity, from which we deduce that the volume of adsorbed water for the 89% data is ≈90 μL. It was this measurement that lead us to use a mass of 80 mg for the PDMS experiments. (The density of PDMS varies from 0.92 to 0.97 g/cc.)

Let us examine the behavior of this high-humidity system further. In Fig. 12 we show the poles and residues of the

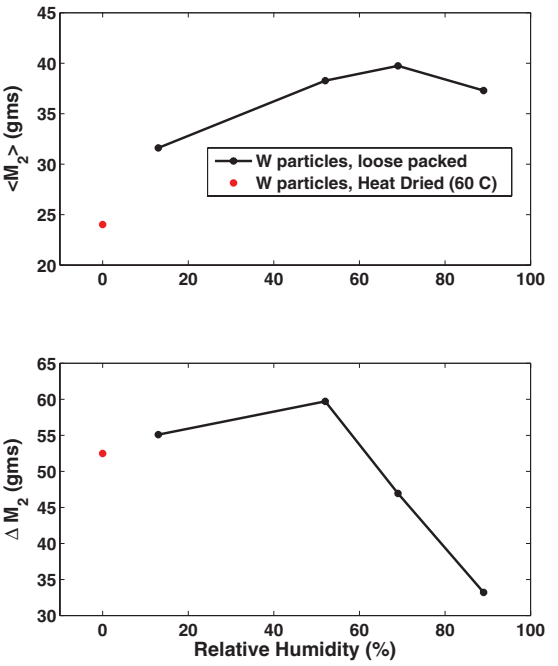

FIG. 11. (Color online) Statistical properties of M_2 computed over the frequency range of the experiment as a function of humidity. (Top) Average; (bottom) standard deviation.

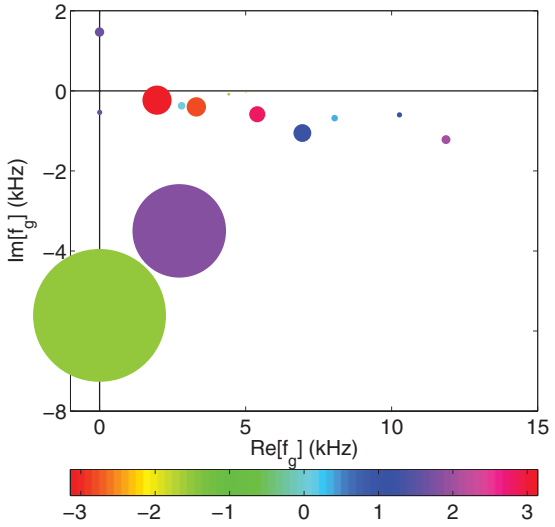

FIG. 12. (Color online) Locations of the normal-mode frequencies which contribute to the pole expansion of the effective mass data for the tungsten granules measured at a relative humidity of 89%. Same conventions as in Fig. 4. This system has one overdamped and one heavily damped mode.

effective mass data for a relative humidity of 89%. Clearly, this system differs from those with PDMS coating.

In addition to the weakly damped modes that we have discussed previously, there is a heavily damped mode at $f_n = [\pm 2726 - 3498i]$ (Hz) and an overdamped mode at $f_n = -5612i$ (Hz), each of which has a large magnitude residue. In Fig. 13 we show the decomposition of this data set into its pole constituents and we explicitly show the contribution that these two damped modes make to the total. [There are also two other modes whose frequencies are purely imaginary, but their residues are so small they make little contribution to $\tilde{M}(\omega)$.] As can be seen from Fig. 13 the contribution of these heavily damped modes to $\tilde{M}(\omega)$ is considerable. We have not seen anything like this in any of our other data sets. We surmise

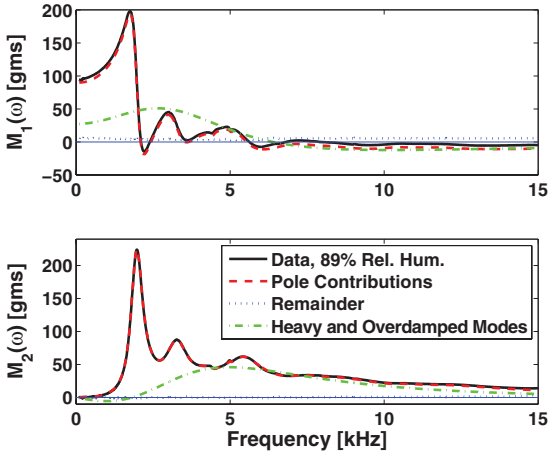

FIG. 13. (Color online) Comparison of measured effective mass data for the 89% relative humidity sample against that deduced from the pole decomposition algorithm of Sec. IV. Same conventions as in Fig. 3 except that we explicitly show the contribution of the overdamped and heavily damped modes separately.

that the water has interacted chemically with the tungsten and formed a material whose attenuative properties are not simply related to the macroscopic viscosity of water. In fact, if the grains are exposed to water for about 1 week, then their appearance becomes visually changed. An elemental analysis of the surface chemistry indicates the presence of oxygen, presumably in the form WO_3. (The data presented in Fig. 13 were taken just under 24 h after sample preparation.) Our conclusion is that there is an attenuation mechanism at play in the high-humidity systems which is not simply related to the bulk viscosity of water but is due, perhaps, to a complex hydrated species of tungsten.

VI. CONCLUSIONS

By means of a combination of experimental and theoretical results on the properties of the effective mass of granular media to attenuate sound we have learned the following:

(i) There exists a level of attenuation apparent in the fundamental mode of the granular medium which is independent of the properties of any adsorbed or coating film. This value, seen in the attenuation of heat-treated tungsten grains, is about the same as that seen in the PDMS-coated grains, extrapolated to zero viscosity, and in that seen in the humidity-controlled studies, extrapolated to zero humidity. We suppose this attenuation is due to physically bonded adsorbents, analogous to the situation seen in the attenuation of rocks. If so, these adsorbents can be removed by heat treating, at high temperatures, in vacuum, for lengthy periods of time [16].

(ii) The attenuation, not only of the fundamental resonance but also those of the others, can be significantly increased either by increasing PDMS viscosity, for a fixed volume of coating fluid in the one set of experiments, or by increasing the volume of adsorbed water by increasing the relative humidity in the other.

(iii) All the modes in the PDMS systems and most of the modes in the humidity-controlled systems are in the weak damping limit in the sense of Sec. III B. The humidity-controlled systems typically have one or more heavily damped modes in addition to the weakly damped ones. In the case of the 89% relative humidity data the contributions of heavily damped and overdamped modes to $\tilde{M}(\omega)$ is quite significant. None of these granular media systems can be said to be equivalent to a high-viscosity fluid as we had hypothesized earlier [3], as this situation would correspond to a sequence of poles on the negative imaginary axis as we discuss in Appendix B.

(iv) The DC viscosity of PDMS increases as the chain length of the constituent molecules increases. This behavior manifests itself in an increase in the attenuation of each of the modes in $\tilde{M}(\omega)$ up to a point. For long-enough chain lengths the dynamic viscosity of PDMS for frequencies in the range of our normal-mode frequencies stops increasing with further chain length increase. It is for this reason that the measured attenuation of the granular normal modes also stops increasing.

(v) The (real part of) the fundamental resonance frequency in the PDMS-controlled experiments does not exhibit any systematic dependence on PDMS chain length, which is understandable on general grounds based on Eq. (51) and the

discussion following. The shear modulus of any of the PDMS fluids is too small to make a significant contribution to the stiffness of the contact and the surface tension of all these films is about the same. In the humidity-controlled experiments there does seem to be a more significant effect on this resonance frequency, as we have observed previously [3]. We suppose this is due to the changing geometry of the adsorbed film and the resulting change in surface tension effects on the contact stiffnesses.

(vi) The attenuation of the fundamental mode in the sample at 89% relative humidity is significantly larger than that of any of the PDMS-controlled experiments, even though the volumes of fluid films are quite similar. Overall, the average values for $\langle M_2 \rangle$ are fairly similar, as one might expect for the weak damping limit.

We are puzzled by two observations. One is that the attenuation of the fundamental mode in the 89% humidity sample is much larger than those of any of the PDMS-coated samples, even though the fluid volumes are nearly the same and all the PDMS fluids are much more viscous than water. Furthermore, we observe a heavily damped and an overdamped mode in the 89% humidity data, but no such modes in any of the PDMS samples. We have ensured that our measurements are always in the small-amplitude limit where linear response theory applies. This fact rules out any nonlinear attenuation mechanism, such as the making and breaking of capillary bonds, as being a major contributor to the attenuation. We understand that the distribution of fluid in the region of the contacts in the PDMS system is not literally the same as in the humidity-controlled one; the latter is at an undersaturated vapor pressure so the liquid forms only in the narrowest of crevices and does not coat the grains.

ACKNOWLEDGMENTS

We greatly appreciate a very insightful discussion with T. Habashy. We are grateful for illuminating discussions on a variety of topics with H. Makse.

APPENDIX A: SPECIFIC EXAMPLE OF THE POLES AND RESIDUES OF A DISCRETE SYSTEM

We consider a one-dimensional string of point masses, separated a distance b from each other, each of which experiences a drag force proportional to the difference between its velocity and its neighbor's, viz.: $F = \gamma[v_j - v_i]$. This leads to the equation of motion for the following ensemble:

$$-m\omega^2 u_j = -i\omega\gamma(u_{j+1} - 2u_j + u_{j-1}) \quad j = -N, \ldots N, \tag{A1}$$

subject to the boundary condition at the side walls

$$u_{\pm(N+1)} = W. \tag{A2}$$

Equation (A1) is a simple example of Eq. (5) in which $B_{ij} = \gamma$ if i and j are nearest neighbors and $K_{ij} \equiv 0$. We introduced this model in Ref. [3] as a discrete version of the Navier-Stokes equation appropriate to a viscous fluid entrained between two parallel walls. In this appendix we use it to demonstrate, explicitly, the decomposition of the effective mass into the sum of its pole contributions, Eq. (22). This model is an example of those discussed in Sec. III C.

It is simple enough to solve for the effective mass implied by this toy model. There are solutions to Eq. (A1) given by

$$u_j = Ay_+^j + By_-^j, \tag{A3}$$

where

$$y_\pm = \frac{2\gamma - im\omega \pm i\sqrt{m^2\omega^2 + 4im\omega\gamma}}{2\gamma}. \tag{A4}$$

Note that $y_- = 1/y_+$. The constants A and B are determined by the boundary conditions, Eq. (A2),

$$A = B = \frac{W}{y_+^{N+1} + y_-^{N+1}}. \tag{A5}$$

The dynamic effective mass is determined from the definition, Eq. (7), using Eqs. (A3)–(A5). The result is

$$\tilde{M}_{1D}(\omega) = \frac{2i\gamma}{\omega}\left[\frac{y_+^{N+1} + y_-^{N+1} - y_+^N - y_-^N}{y_+^{N+1} + y_-^{N+1}}\right]. \tag{A6}$$

As there are $2N+1$ particles in the system there are $2N+1$ normal modes. Of these, N of them are antisymmetric ($u_j = -u_{-j}$). They do not contribute to the effective mass, so we do not consider them here. The remaining $N+1$ normal modes are symmetric ($u_j = +u_{-j}$); they correspond to the vanishing of the denominator of Eq. (A6):

$$y_+^{N+1} = -y_-^{N+1}. \tag{A7}$$

Let

$$\theta_k = \frac{(2k+1)\pi}{N+1} \quad k = 0,1,2,\ldots,N-1,N. \tag{A8}$$

Then a symmetric normal mode is defined by taking the $N+1$ root of Eq. (A7):

$$y_+ = e^{i\theta_k} y_- = e^{i\theta_k/2}, \tag{A9}$$

where the second equation follows because $y_+ = 1/y_-$. By means of the definitions given in Eq. (A4), we may solve for the normal-mode frequencies all of which lie on the negative imaginary axis, $\omega_k = -i\beta_k$. We find

$$\beta_k = \frac{4\gamma}{m}\sin^2(\theta_k/4) \quad k = 0,1,2,\ldots,N-1,N. \tag{A10}$$

The k-th (un-normalized) symmetric normal mode is given by Eq. (A3) with $A = B$: $u_j = y_+^j + y_+^{-j}$, i.e.,

$$e_j^{(k)} = \cos(j\theta_k/2) \quad j = -N,\ldots,N. \tag{A11}$$

It is straightforward, if tedious, to derive closed form expressions for all the sums over particle displacements indicated in Eqs. (23) and (38). The result is

$$A_k = i4\gamma\frac{\sin[(N+1/2)\theta_k/2]\sin(\theta_k/2)\cos(N\theta_k/2)}{\sin(\theta_k/4)\{\sin[(2N+1)\theta_k/2] + (2N+1)\sin(\theta_k/2)\}}. \tag{A12}$$

The pole decomposition of Eq. (A6) is

$$\tilde{M}_{\text{pole}}(\omega) = \sum_{k=0}^{N}\frac{A_k}{\omega + i\beta_k}. \tag{A13}$$

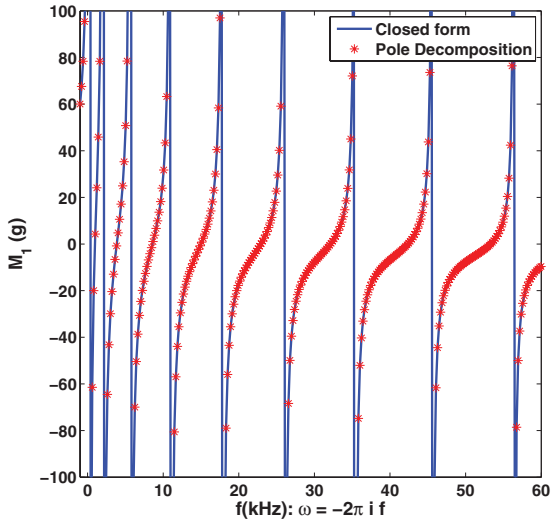

FIG. 14. (Color online) Comparison of two equivalent expressions for the effective mass of the 1D model, Eqs. (A6) and (A13), plotted on the negative imaginary frequency axis. Here, $N = 18$, $\gamma = 1.20 \times 10^6$, and $m = 5.65$. The imaginary part of $\tilde{M}$ is zero on the imaginary axis.

These two functions, given by Eqs. (A6) and (A13), are plotted together in Fig. 14 for frequencies on the negative imaginary axis where all the poles reside. We see that they do, indeed, overlie each other.

APPENDIX B: A TEST OF THE DECOMPOSITION ALGORITHM

In Sec. IV we have presented an algorithm with which we deduce the poles and residues of a causal response function from experimental data taken at a finite number of real-valued frequencies. In this Appendix we test the validity of this procedure on an analytic function whose poles and residues can also be derived analytically. The function we use is one which has some of the features of our actual experimental data, namely the function denoted as Model I in Ref. [3]. It is

$$\tilde{M}_I(\omega) = M_0 \frac{\tan(qL)}{qL}, \tag{B1}$$

where $q = \frac{\omega}{c_0\sqrt{(1-i\omega\tau)}}$. This function describes reasonably well the effective mass of a simple liquid, having sound speed c_0 and damping parameter τ, and which fills the cavity to a height L.

If the damping parameter, τ, vanishes, then the resonance frequencies are all real-valued and have the simple form:

$$\omega_n^0 = (2n-1)\frac{\pi}{2}\frac{c_0}{L} \quad n = 1,2,3,\ldots, \tag{B2}$$

and the negatives thereof. If $\tau \neq 0$, then for large enough n Eq. (B2) cannot be even approximately correct. It is simple enough to solve for those normal-mode frequencies by setting the argument of the tangent function equal to an odd multiple of $\pi/2$. The result is

$$\omega_n^{\pm} = \pm\omega_n^0\sqrt{1-\left(\omega_n^0\tau/2\right)^2} - i\left(\omega_n^0\right)^2\tau/2. \tag{B3}$$

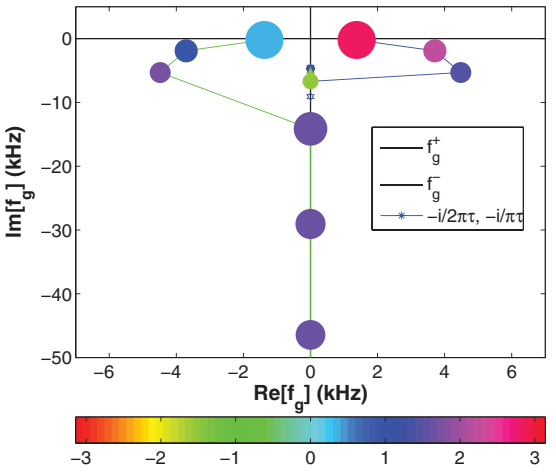

FIG. 15. (Color online) Poles and the corresponding residues of the simple effective mass, Eq. (B1). The exact locations are given by Eqs. (B3) and the exact residues by (B6). The area of each solid circle is proportional to $|A_n^{\pm}|$ and the color is its phase according to the color bar (in radians).

In order to deduce the residues of these poles we use the identity [17],

$$\tan(\theta) = \sum_{n=1}^{\infty} \frac{2\theta}{[(2n-1)\pi/2]^2 - \theta^2}. \tag{B4}$$

After a bit of rearranging Eq. (B1) may be written in terms of its pole contributions as

$$\tilde{M}_I(\omega) = \sum_{n=1}^{\infty}\left[\frac{A_n^+}{\omega-\omega_n^+} + \frac{A_n^-}{\omega-\omega_n^-}\right], \tag{B5}$$

where

$$A_n^{\pm} = \pm\frac{M_0 c_0^2}{L^2}\frac{(\omega_n^{\pm})^2}{\left(\omega_n^0\right)^3\sqrt{1-\left(\omega_n^0\tau/2\right)^2}}. \tag{B6}$$

For a specific choice of the three parameters $M_0 = 149$ g, $c_0 = 171$ m/s, $\tau = 35$ μs, and $L = 3.07$ cm, we plot the

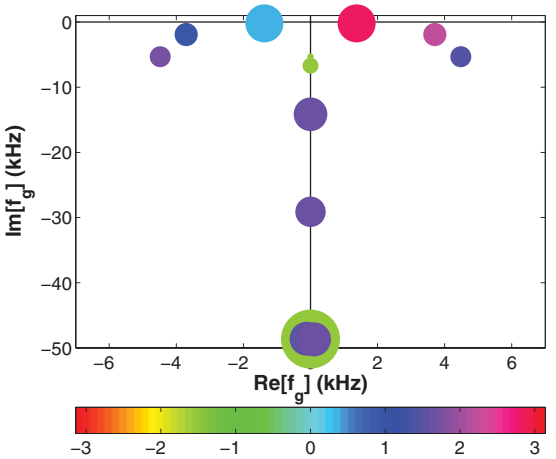

FIG. 16. (Color online) Poles and residues of the simple effective mass, Eq. (B1), using numerically generated data. This picture is virtually identical to that of Fig. 15.

exact expressions for the poles and their residues in Fig. 15. Although $\tilde{M}_I(\omega)$ is intended to describe a continuum effective mass we see that, for small-enough values of n, the normal-mode frequencies are nearly real valued, but, for $n > [1 + 4L/(c_0\tau\pi)]/2$, the normal-mode frequencies and their residues are purely imaginary, as we hypothesized at the end of Sec. III. We note that for weak damping $\omega_n^0\tau \ll 1$, the poles and their residues follow Eqs. (32) and (33), respectively. For large enough n, $\omega_n^0\tau \gg 1$, the "+" branch has an accumulation point: $\omega_{n\to\infty}^{+} = -i/\tau$. In this limit the residues of those poles, however, tend to zero $A_{n\to\infty}^{+} \propto n^{-4}$ and they make a negligible contribution to $\tilde{M}_I(\omega)$. In this same large n limit, the other, "−", branch has poles and residues which follow Eqs. (37) and (39). It is these poles and residues that give rise to the high-frequency behavior of Eq. (B1) on the real axis: $\lim_{\omega\to\infty} \tilde{M}_I(\omega) \propto (-i\omega)^{-1/2}$.

We have proposed a means of deducing the normal-mode frequencies and their residues from our experimental data, in Sec. IV. In order to test the validity of this procedure we have generated 1500 data points directly from Eq. (B1) which are equally spaced between 100 Hz and 15 kHz, as for our experimental procedure. We use these "data" as input to the procedure of Sec. IV. The results are shown in Fig. 16, which are to be compared against the exact results shown in Fig. 15. Except for the modal frequency around $-i50$ kHz, our procedure works well in determining the complex-valued normal-mode frequencies and their residues. The procedure even works well in determining some of the small residue poles of the "+" branch. Thus, we conclude that, as long as the sought-after poles lie within the rectangle $[\pm 15 \text{ kHz}, \pm i15 \text{ kHz}]$, our procedure will determine their properties with a reasonable accuracy.

[1] L. Cremer and M. Heckl, *Structure Borne Sound* (Springer, Berlin, 1973).

[2] J. M. Bourinet and D. Le Houèdec, Comput. Struct. **73**, 395 (1999); J. C. Sun, H. B. Sun, L. C. Chow, and E. J. Richards, J. Sound Vib. **104**, 243 (1986); S. A. Nayfeh, J. M. Verdirame, and K. K. Varanasi, Proc. SPIE **4697**, 158 (2002); K. K. Varanasi and S. A. Nayfeh, *Proceedings of the DETC 2003 ASME Design Eng. Technical Conference* (Montreal, 2003, unpublished).

[3] J. Valenza, C.-J. Hsu, R. Ingale, N. Gland, H. A. Makse, and D. L. Johnson, Phys. Rev. E **80**, 051304 (2009); J. J. Valenza, C.-J. Hsu, and D. L. Johnson, J. Acoust. Soc. Am. **128**, 2768 (2010).

[4] J. N. D'Amour, J. J. R. Stålgren, K. K. Kanazawa, C. W. Frank, M. Rodahl, and D. Johannsmann, Phys. Rev. Lett. **96**, 058301 (2006).

[5] Th. Brunet, X. Jia, and P. Mills, Phys. Rev. Lett. **101**, 138001 (2008).

[6] C. S. O'Hern, L. E. Silbert, A. J. Liu, and S. R. Nagel, Phys. Rev. E **68**, 011306 (2003); L. E. Silbert, A. J. Liu, and S. R. Nagel, Phys. Rev. Lett. **95**, 098301 (2005); K. Chen, W. G. Ellenbroek, Z. Zhang, D. T. N. Chen, P. J. Yunker, S. Henkes, C. Brito, O. Dauchot, W. van Saarloos, A. J. Liu, and A. G. Yodh, *ibid.* **105**, 025501 (2010).

[7] C. F. Schreck, T. Bertrand, C. S. O'Hern, and M. D. Shattuck, Phys. Rev. Lett. **107**, 078301 (2011).

[8] C. Song, P. Wang, and H. A. Makse, Nature **453**, 629 (2008).

[9] J. Brujic, P. Wang, C. Song, D. L. Johnson, O. Sindt, and H. A. Makse, Phys. Rev. Lett. **95**, 128001 (2005).

[10] J. B. Knight, C. G. Fandrich, C. N. Lau, H. M. Jaeger, and S. R. Nagel, Phys. Rev. E **51**, 3957 (1995); E. R. Nowak, J. B. Knight, M. L. Povinelli, H. M. Jaeger, and S. R. Nagel, Powder Technol. **94**, 79 (1997); E. R. Nowak, J. B. Knight, E. Ben-Naim, H. M. Jaeger, and S. R. Nagel, Phys. Rev. E **57**, 1971 (1998).

[11] J. H. Wilkinson, *Algebraic Eigenvalue Problem* (Oxford University Press, New York, 1965).

[12] W. J. Tzeng and F. Y. Wu, J. Phys. A: Math. Gen. **39**, 8579 (2006).

[13] W. H. Press, B. P. Flannery, S. A. Teukolsky, and W. T. Vetterling, *Numerical Recipes* (Cambridge University Press, New York, 1987).

[14] A. J. Barlow, G. Harrison, and J. Lamb, Proc. R. Soc. London A **282**, 228 (1964).

[15] B. B. Sauer and G. T. Dee, Macromolecules **24**, 2124 (1991).

[16] B. R. Tittmann, V. A. Clark, and J. M. Richardson, J. Geophys. Res. **85**, 5199 (1980).

[17] L. L. Smail, in *Elements of the Theory of Infinite Processes* (McGraw-Hill, New York, 1923), p. 237; L. B. W. Jolley, in *Summation of Series*, 2nd ed. (Dover, New York, 1961), p. 144.